NANO LETTERS

Letter

pubs.acs.org/NanoLett

Nanosecond Spin Lifetimes in Single- and Few-Layer Graphene–hBN Heterostructures at Room Temperature

Marc Drögeler,[†] Frank Volmer,[†] Maik Wolter,[†] Bernat Terrés,[†,‡] Kenji Watanabe,[¶] Takashi Taniguchi,[¶] Gernot Güntherodt,[†] Christoph Stampfer,[†,‡] and Bernd Beschoten*[,†]

[†]2nd Institute of Physics and JARA-FIT, RWTH Aachen University, 52074 Aachen, Germany

[‡]Peter Grünberg Institute (PGI-9), Forschungszentrum Jülich, 52425 Jülich, Germany

[¶]National Institute for Materials Science, 1-1 Namiki, Tsukuba, 305-0044, Japan

Supporting Information

ABSTRACT: We present a new fabrication method of graphene spin-valve devices that yields enhanced spin and charge transport properties by improving both the electrode-to-graphene and graphene-to-substrate interface. First, we prepare Co/MgO spin injection electrodes onto Si^{++}/SiO_2. Thereafter, we mechanically transfer a graphene–hBN heterostructure onto the prepatterned electrodes. We show that room temperature spin transport in single-, bi-, and trilayer graphene devices exhibit nanosecond spin lifetimes with spin diffusion lengths reaching 10 μm combined with carrier mobilities exceeding 20 000 $cm^2/(V\ s)$.

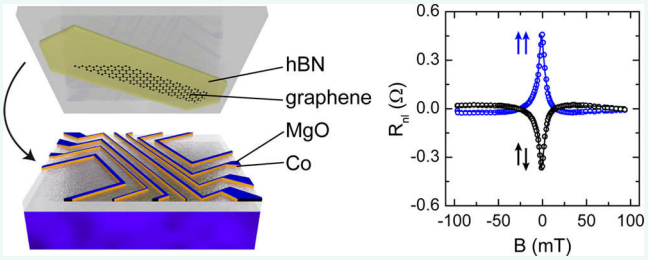

KEYWORDS: *Graphene, boron nitride, spin transport, Hanle precession*

In recent years, graphene has drawn strong attention because of measured spin-diffusion lengths of several microns at room temperature. Typical nonlocal spin-valve devices on Si/SiO_2 substrates with charge carrier mobilities of several thousand $cm^2/(V\ s)$ exhibit spin lifetimes below 1 ns.[1−10] In contrast, room temperature spin lifetimes above 1 ns have only been observed for epitaxial graphene on SiC (ref 11) and for bilayer graphene devices (BLG) with low carrier mobility of 300 $cm^2/(V\ s)$ (ref 2) or after postprocessing of as-fabricated devices either by hydrogenation[12] or by oxygen treatment[13] that both, however, result in a decrease of the mobility. In graphene-based spintronics, there is a device-oriented quest for combining long spin lifetimes with large carrier mobilities. While large carrier mobilities have been achieved in suspended structures[14] and spin-valves on hexagonal boron nitride (hBN) crystals,[15] the respective spin lifetimes only exhibit several 100 ps. Recent studies indicate that the overall short spin lifetimes are most likely not a result of intrinsic spin scattering mechanisms in graphene but are rather caused and limited by the contact and interface properties of spin injection and detection electrodes.[4,9,16] This notion is supported by the observed increase of the spin lifetime with the contact-resistance-area products (R_cA) of both single-layer (SLG) and BLG devices.[4,13] In this context, it is important to note that the oxide barrier, which is needed for spin injection and detection, usually does not grow epitaxially on the graphene surface. MgO, for example, grows in a Volmer–Weber mode (island formation) if no additional wetting layer is used.[17] This island growth yields rather rough surfaces and additionally favors the formation of conducting pinholes between the overlaying ferromagnetic metal that is subsequently deposited and the underlaying graphene sheet. It has been suggested that these conducting pinhole states may be the bottleneck for spin transport when hybridizing with the graphene layer.[4]

In this Letter, we present a new pathway for fabricating graphene spin-valves that diminishes some of the aforementioned shortcomings of the spin injection and detection contacts. In our approach, we first pattern MgO/Co electrodes that are deposited onto a silicon substrate. We emphasize that in contrast to all previous methods our MgO barrier is not deposited onto graphene but rather on top of the ferromagnetic Co layer. Thereafter, we mechanically press a graphene flake, which was previously transferred on hBN, onto the MgO surface of the electrodes. We show that this transfer technique allows for (1) nanosecond spin lifetimes with values up to 3.7 ns in trilayer graphene (TLG) devices which result from large (R_cA) values of the contacts and at the same time for (2) high carrier mobilities according to the enhanced charge transport properties by the mechanical contact of graphene to the overlaying flattening hBN layer.

The new sample fabrication consists of two main steps (see Figure 1a,b) quite in contrast to the previously used top-down process. In a first step, we prepare Co/MgO electrodes on a Si^{++}/SiO_2 substrate, where the Si^{++} can be used as a back gate.

Received: April 7, 2014
Revised: August 21, 2014
Published: September 10, 2014

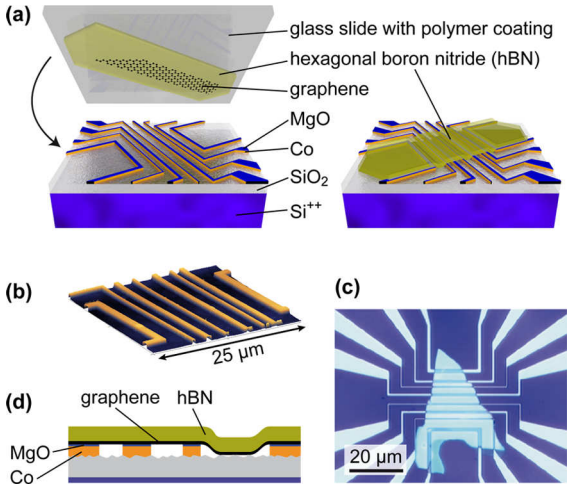

Figure 1. (a) Transfer technique for fabricating nonlocal graphene spin-valves (similar to ref 18). (b) Scanning force microscope image of the prepared ferromagnetic electrodes. (c) Optical micrograph of a transferred graphene–hBN heterostructure onto MgO/Co electrodes. (d) Schematic cross-section of the final device.

The electrodes are defined by standard electron beam lithography and metallized by molecular beam epitaxy. We use 40 nm thick Co for spin injection and detection. Afterward, we deposit 1 nm of MgO on top of the Co. This layer acts as an injection barrier to allow for efficient spin injection and detection. A scanning force microscopy (SFM) image of the prepared electrodes is shown in Figure 1b. The electrodes exhibit smooth surfaces and do not show fencing at their edges. Both are essential for a plain graphene-to-electrode interface.

The second step is illustrated in Figure 1a. We use exfoliated hBN that was transferred onto a glass slide covered by a polymer to pick up exfoliated graphene from a second Si^{++}/SiO_2 substrate (similar technique as described by Wang et al.[18]). The thickness of the hBN varies between 60–80 nm. Subsequently, the graphene–hBN heterostructure is mechanically transferred on top of the electrodes and the glass slide is thereafter removed by dissolving the polymer in acetone. A top-view optical image of the finished device is shown in Figure 1c.

As illustrated by the cross-section of our device (Figure 1d), the graphene–hBN heterostructure is suspended for small electrode spacings while it may bend down to the underlying SiO_2 surface (nonsuspended) for larger spacings. The bending can easily be seen in the optical image in Figure 2a of a different SLG device where the optical contrast is encoded into a false-color scheme (orange for suspended and green for non-suspended), which even visualizes the underlaying graphene flake. An additional SFM line scan (Figure 2c) perpendicular to the electrodes in Figure 2d confirms this assignment.

To further analyze the quality of our transferred SLG-hBN heterostructure, we use micro-Raman spectroscopy to compare suspended with nonsuspended regions. The respective spectra in Figure 2b have been taken at the positions of the black and red crosses in Figure 2a. We observe three distinct peaks which can be attributed to hBN and the G- and 2D-line of graphene. For suspended graphene (black curve), we get peak positions (G-peak at 1583 cm^{-1} and 2D-peak at 2679 cm^{-1}) that are very close to the values for pristine, free-standing graphene.[19] For the nonsuspended graphene regions, however, we find a strong shift of both peak positions to larger wave numbers (red curve). This shift can be explained by local changes in doping and strain.[19]

We therefore recorded a Raman map over the device area shown in Figure 2d and use a vector decomposition of the G- and the 2D-peak shift[19] to estimate doping and strain distributions in the graphene that are plotted in Figure 2e,f, respectively. We note that this method only determines the carrier density but not its type.[19,20] For the suspended parts of the graphene flake, there are only minor charge fluctuations (<5 × 10^{11} cm^{-2}) visible while rather high doping is observed in all areas which are in direct contact with the electrodes. Moreover, doping occurs in the nonsuspended regions that are in direct contact to the SiO_2 substrate. The doping may result from vacancies or charged defects in the MgO/Co electrodes and in the substrate exhibiting local electric fields which cause local doping.[21,22]

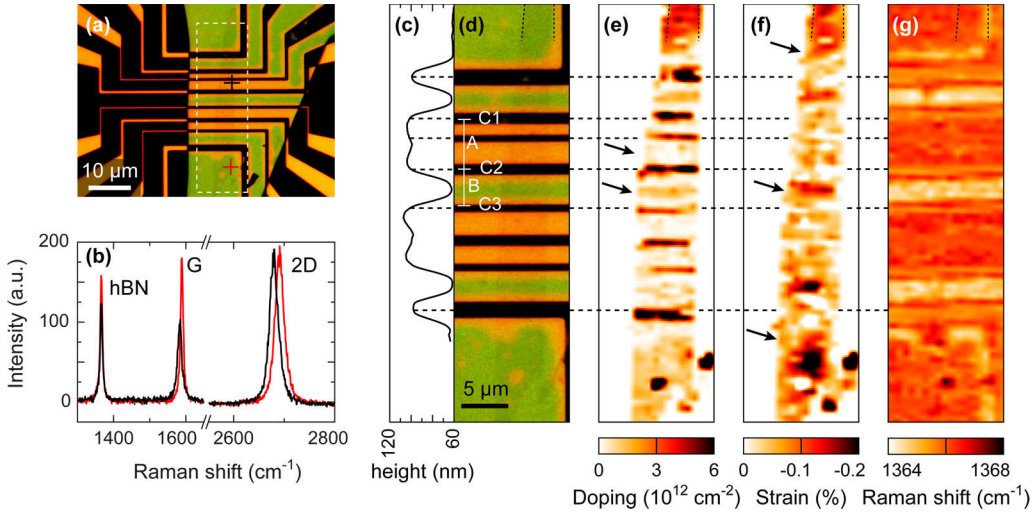

Figure 2. (a) Top view optical image of a Co/MgO/SLG-hBN device. (b) Raman spectra taken at the black and red crosses in panel (a). (c) SFM height profile scan showing the bending of the SLG-hBN. (d) Close up of white rectangular image detail in panel (a). (e) Doping and (f) strain distribution of the graphene flake. Values are extracted from the G- and 2D-line positions of the Raman maps following ref 19. (g) Spatial image of the Raman hBN peak position (see panel (b)).

dx.doi.org/10.1021/nl501278c | Nano Lett. 2014, 14, 6050–6055

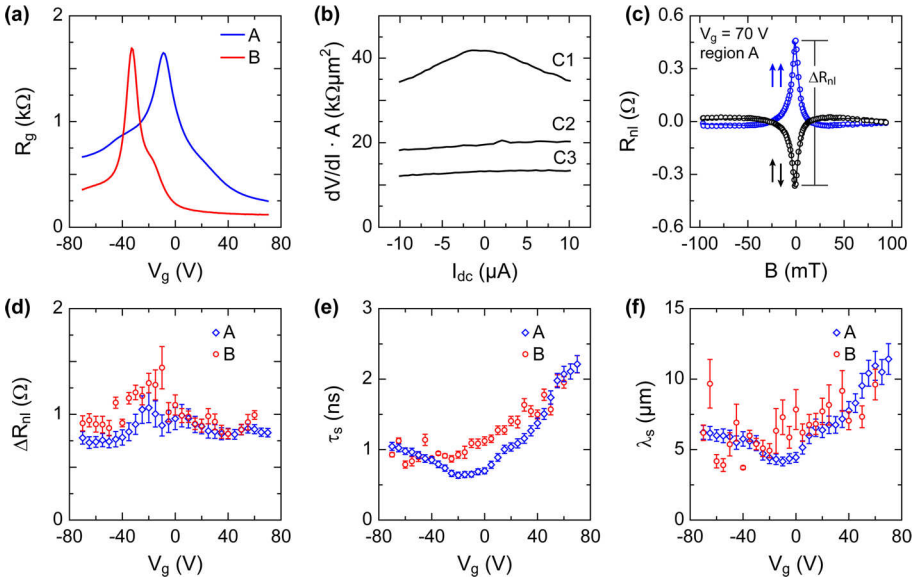

Figure 3. (a) Gate dependent graphene resistance of the SLG device from Figure 2 for suspended region A (blue curve) and nonsuspended region B (red curve). (b) $dV/dI \cdot A$ curves of contacts C1, C2, and C3 labeled in Figure 2d. (c) Hanle spin precession curves taken at $V_g = 70$ V in region A. (d) Gate dependent spin signal for region A (blue data points) and region B (red data points). Respective gate dependent spin lifetimes are shown in panel (e) and spin diffusion lengths in panel (f).

The local strain distribution is shown in Figure 2f. There is only small strain in suspended regions and in regions that are supported by the electrodes. However, we find larger strain values in the nonsuspended regions that may either result from the bending of the graphene (see Figure 2c) or is a substrate-induced effect. It is thus interesting to explore whether the larger strain has any influence on the spin transport properties.[23] Furthermore, we note that the largest strain is measured in areas where graphene has direct contact to the SiO_2 surface (see arrows in Figure 2f). These findings are in agreement with previous results by Lee et al. for graphene on SiO_2,[19] demonstrating that graphene exhibits less strain on hBN compared to SiO_2 substrates. The bending of the graphene–hBN heterostructure can also be seen as a peak shift of the hBN Raman line (Figure 2g), which can also be explained by local strain.[24]

We next focus on spin and charge transport measurements on the SLG device presented in Figure 3. All transport measurements were performed at room temperature under vacuum conditions using a standard low-frequency lock-in technique.[25] In Figure 3a, we show the four-terminal back gate dependent resistance of the suspended region A (blue curve) and the nonsuspended region B (red trace) (for assignment see Figure 2d). The charge neutrality point (CNP) of the suspended region is close to zero gate voltage while it is shifted to $V_g = -34$ V for the nonsuspended region. The shift of the latter results from a strong n-doping by the substrate whereas the suspended region A is only slightly doped which is both in accordance to the Raman analysis in Figure 2e.

We extract the carrier density by $n = \alpha(V_g - V_g^0)$ with V_g being the back gate voltage and V_g^0 being the voltage to reach the CNP. The capacitive coupling constant α is different for suspended and nonsuspended regions with respective values of $\alpha_A = 3.5 \times 10^{10}$ V^{-1} cm^{-2} and $\alpha_B = 4.8 \times 10^{10}$ V^{-1} cm^{-2}.[26]

The electron mobilities μ are determined from the gate dependent conductance σ using $\mu = 1/e \cdot \Delta\sigma/\Delta n$. We obtain mobilities of 23 000 cm^2/(V s) for the suspended region A and 20 000 cm^2/(V s) for the nonsuspended region B near the CNP. Compared to all previous room temperature carrier mobilities in graphene spin-valve devices on Si/SiO_2 substrates these values are more than a factor of 2 larger that highlights the high quality of our devices.[2] We note that the given analysis is oversimplified as the graphene parts that are residing on top of the electrodes cannot be tuned by the gate voltage due to shielding of the back gate fields by the electrodes. The respective graphene resistance is thus a gate-independent contribution to the total graphene resistance. This results in a smaller slope of σ versus V_G and thereby yield smaller mobilities when using the above conservative estimate.

We characterize all spin injection and detection electrodes (C1 to C3) of regions A and B (see Figure 2d) by their differential contact-resistance-area product ($dV/dI \cdot A$) with A being the respective contact area.[4] As the electrodes can be contacted from both sides of the graphene flake, we use a four-terminal measurement of the contact resistance (see also ref 4). To determine the differential contact resistance we use a dc current that is modulated by a small ac current and detect the ac filtered voltage drop. We observe large values for all contacts (Figure 3b). Only contact C1 exhibits the typical cusp-like dependence indicating tunneling behavior while the other contacts show a flat $dV/dI \cdot A$ curve that indicates transparent barriers. Interestingly, in previous studies transparent contacts could only be observed for contact-resistance-area products below 1 kΩ μm^2 for devices with a rather thick MgO layer (2–3 nm) that was directly deposited onto graphene.[4] We thus conclude that our thinner MgO barriers (1 nm) have better contact properties that might be explained by the weaker coupling to the graphene layer after the mechanical transfer of the graphene–hBN heterostructure onto the MgO surface.

Spin transport properties were measured in the standard four-terminal nonlocal Hanle geometry.[1,27,28] A typical measurement is shown in Figure 3c for region A at $V_g = 70$ V for parallel and antiparallel alignments of the Co magnetizations of the respective injector and detector electrodes after background subtraction. The spin signal ΔR_{nl} is given by the resistance difference at $B = 0$ T. The Hanle

dx.doi.org/10.1021/nl501278c | Nano Lett. 2014, 14, 6050–6055

depolarization curves are fitted by a simplified solution of the steady-state Bloch-Torrey equation[29−31]

$$\frac{\partial \vec{s}}{\partial t} = \vec{s} \times \vec{\omega}_0 + D_s \nabla^2 \vec{s} - \frac{\vec{s}}{\tau_s} = 0 \quad (1)$$

where $\vec{s}$ is the net spin vector, D_s is the spin diffusion constant, and τ_s is the spin lifetime. Additionally, $\vec{\omega}_0 = g\mu_B \vec{B}/\hbar$ represents the Larmor frequency, where μ_B is the Bohr magneton, $\vec{B} = \vec{B}_\perp$ is the out-of-plane magnetic field and $g = 2$ is the gyromagnetic factor. The spin diffusion length λ_s is given by $\lambda_s = (D_s\tau_s)^{1/2}$. The solution assumes one-dimensional transport, delta-like injectors and detectors. This analysis yields an averaged spin lifetime for the whole graphene layer from the injector to the detector contact. We note, however, that the spin lifetime in graphene that is covered by contacts may significantly differ from bare graphene parts between those contacts in particular for devices with low contact-resistance-area products.[13,14]

In Figure 3d, we show ΔR_{nl} as a function of V_g for the suspended region A (blue diamonds) and the nonsuspended region B (red circles). Spin-valve switching curves are shown in the Supporting Information. For both regions, the spin signal is on the order of 1 Ω and shows a slight increase near the CNP. According to Han et al. this increase is characteristic for tunneling contacts.[9] However, as seen in Figure 3 two of the three electrodes show a flat dV/dI-curve, which indicates transparent contacts with potential pinholes. We thus find that the gate dependence of the spin signal alone is not an unambiguous sign for the tunneling behavior of the contact.

In Figure 3e, we plot the respective gate dependent spin lifetimes τ_s. Most strikingly, we observe a strong increase of τ_s toward electron doping for $V_g > 0$ V with maximum values exceeding 2 ns. The enhanced spin transport properties are also seen in the spin diffusion lengths that exceed 10 μm in both suspended and nonsuspended regions (see Figure 3f). The latter values are larger than in all previous measurements on nonlocal spin-valves including results on hBN (4.5 μm)[15] and hydrogenated graphene (7 μm).[12] The enhanced spin transport properties for increased doping values have also been observed in most previous experiments,[2,3,6,7,10,15,32] but their origin is not completely understood.[33−35] Surprisingly, there is no distinct difference in τ_s and λ_s between the suspended and the nonsuspended region indicating that even in our new devices the spin lifetime may still be limited by contact-induced spin dephasing which hinders to explore intrinsic spin dephasing and spin relaxation mechanisms in the graphene layer itself.

It is interesting to compare these SLG results to few-layer graphene devices. By the same fabrication method we therefore additionally prepared BLG and TLG devices and show results on charge transport and spin lifetimes in Figure 4a,b, respectively. The data were taken on nonsuspended regions that again result in a shift of the CNP toward negative gate voltages (see Figure 4a). We estimate electron carrier mobilities of 9000 cm^2/(V s) for BLG and 10 000 cm^2/(V s) for TLG where we used $\alpha = 4.9 \times 10^{10}$ V^{-1}cm^{-2} for both. As discussed above, these values should be taken as a lower limit estimate. In contrast to the SLG device, we observe a completely different density dependence of the respective spin lifetimes in Figure 4b (see Supporting Information Figures S2 and S3 for respective gate dependent spin signals and spin diffusion lengths). While τ_s depends only weakly on gate voltage, it becomes largest at the CNP reaching 3.7 ns for the TLG device, which is the largest room temperature value in graphene-based nonlocal spin transport to date. A similar gate voltage dependence was previously also observed in other graphene spin-valve devices[7,10,12,15] including SLG. We therefore do not attribute this behavior to the number of graphene layers.

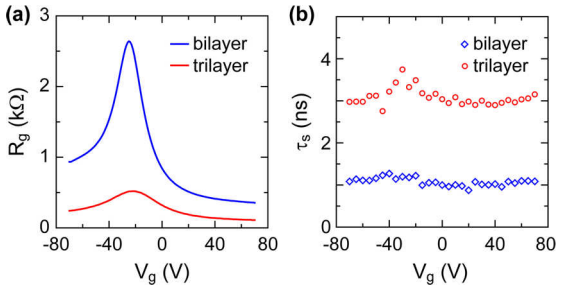

Figure 4. (a) Graphene resistance as a function of gate voltage for nonsuspended BLG (blue curve) and TLG (red curve) devices. (b) Room temperature spin lifetime versus back gate voltage for BLG (blue diamonds) and TLG devices (red circles).

We summarize our results in Figure 5. Figure 5a shows the dependence of τ_s on the electron mobility on a log−log scale.

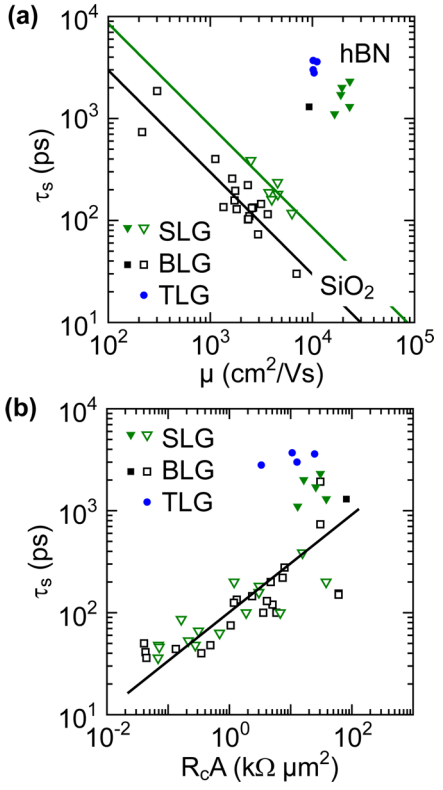

Figure 5. (a) Room temperature spin lifetime as a function of carrier mobility obtained on single- and few-layer graphene nonlocal spin-valve devices for Co/MgO spin injection and detection electrodes. Results from the present study are depicted by the filled symbols while previous results on single and bilayer graphene (open symbols) are taken from refs 2 and 4. The solid lines illustrate the measured $1/\mu$ dependence in SLG and BLG devices with Co/MgO electrodes prepared by the conventional top-down fabrication method. (b) Spin lifetime versus contact-resistance-area product of respective injection and detection electrode at an electron density of $n = 1.5 \times 10^{12}$ cm^{-2} at room temperature (filled symbols). For comparison we included all previous results from ref 4 on SLG and BLG devices that were fabricated by the conventional top-down method. The solid line is a guide to the eye.

dx.doi.org/10.1021/nl501278c | Nano Lett. 2014, 14, 6050−6055

Data points from the present study are shown by filled symbols. In total, we measured 10 regions of 5 devices. In 9 regions, we obtain maximum spin lifetimes above 2 ns and mobilities above 10 000 $cm^2/(V\ s)$ that demonstrates the reproducibility of the device performance by our fabrication method. For easier comparison, we include results on SLG and BLG that some of us had previously measured.[2,4] All latter devices were prepared on Si/SiO_2 by a conventional top-down fabrication method in which the MgO barriers are directly evaporated onto graphene. The overall improvements of the performances of our new devices are striking. These new devices exhibit spin lifetimes that are 2 orders of magnitude longer than the previous BLG devices (squares) with the largest mobility of 8000 $cm^2/(V\ s)$ that only yielded τ_s = 30 ps.[2] While a nanosecond spin lifetime was obtained in BLG devices with mobilities as low as 300 $cm^2/(V\ s)$, we now obtain nanosecond spin lifetimes with mobilities that are almost 2 orders of magnitude larger. We clearly attribute the increase in the mobilities to the hBN substrate while in essence we relate the increase of the spin lifetimes to improved contact (i.e., electrode interface) properties according to our advanced transfer technique onto prepatterned electrodes that has several advantages over previous methods. First, the contact region of the graphene is never exposed to an electron beam, which most likely leads to a smaller number of spin-scattering centers in graphene.[36] Second, the interface between graphene and MgO is expected to be of higher quality, because more aggressive cleaning procedures can be used for removing resist residues from the lithography step. Furthermore, there is an island growth of MgO on graphene[17] whereas it can grow fully epitaxial on Co.[37] Although our present MgO layers do not grow epitaxially, they seem to be more homogeneous than in previous studies. The homogeneity of the MgO layer does not only lead to an improved spin injection efficiency but also prohibits direct contact of Co atoms to graphene that is known to induce 3d-like hybridized states in graphene and can yield strong spin scattering.[38] We finally discuss the dependence of the spin lifetime on the R_cA values in Figure 5b, which includes results from our present (filled symbols) and our previous study (open symbols).[4] As the R_cA values typically vary within a single device, we plot the respective mean values of injector and detector contacts of each device. While we observed a clear increase of τ_s with R_cA for all previous devices (see also solid line as a guide to the eye in Figure 5b), all new devices show significantly longer spin lifetimes with smaller variations in the R_cA values. This finding shows that the contact resistance alone cannot be responsible for the measured spin lifetimes. It rather indicates that the longer spin lifetimes might also result from the enhanced carrier mobilities of graphene (Figure 5a). This notion is also supported by the recent results from Guimaraes et al., who achieved spin lifetimes of 2 ns in fully hBN encapsulated graphene.[39]

In summary, we presented a new way of fabricating graphene–hBN spin-valve devices where we mechanically transfer the graphene onto predefined Co/MgO electrodes. All single-layer, bilayer, and trilayer graphene devices exhibit nanosecond spin lifetimes up to 3.7 ns with carrier mobilities exceeding 20 000 $cm^2/(V\ s)$ and spin diffusion lengths above 10 μm. Our presented transfer method can be applied to epitaxial oxide barriers, which are expected to yield even longer spin lifetimes. This ultimately paves the way to explore intrinsic spin transport properties and to realize promising devices in highest mobility graphene.

■ ASSOCIATED CONTENT

Supporting Information

The Supporting Information contains additional spin-valve switching curves of SLG devices and gate dependent spin transport parameters of BLG and TLG devices as well as dV/dI curves of the respective spin injection and spin detection contacts. This material is available free of charge via the Internet at http://pubs.acs.org.

■ AUTHOR INFORMATION

Corresponding Author

*E-mail: bernd.beschoten@physik.rwth-aachen.de.

Notes

The authors declare no competing financial interest.

■ ACKNOWLEDGMENTS

We thank S. Göbbels for helpful discussions and S. Engels for help with the transfer process. The research leading to these results has received funding from the DFG through FOR-912 and the European Union Seventh Framework Programme under grant agreement no. 604391 Graphene Flagship.

■ REFERENCES

(1) Tombros, N.; Jozsa, C.; Popinciuc, M.; Jonkman, H. T.; van Wees, B. J. *Nature* **2007**, *448*, 571–574.
(2) Yang, T.-Y.; Balakrishnan, J.; Volmer, F.; Avsar, A.; Jaiswal, M.; Samm, J.; Ali, S. R.; Pachoud, A.; Zeng, M.; Popinciuc, M.; Güntherodt, G.; Beschoten, B.; Özyilmaz, B. *Phys. Rev. Lett.* **2011**, *107*, 047206.
(3) Avsar, A.; Yang, T.-Y.; Bae, S.; Balakrishnan, J.; Volmer, F.; Jaiswal, M.; Yi, Z.; Ali, S. R.; Güntherodt, G.; Hong, B. H.; Beschoten, B.; Özyilmaz, B. *Nano Lett.* **2011**, *11*, 2363–2368.
(4) Volmer, F.; Drögeler, M.; Maynicke, E.; von den Driesch, N.; Boschen, M. L.; Güntherodt, G.; Beschoten, B. *Phys. Rev. B* **2013**, *88*, 161405.
(5) Popinciuc, M.; Józsa, C.; Zomer, P. J.; Tombros, N.; Veligura, A.; Jonkman, H. T.; van Wees, B. J. *Phys. Rev. B* **2009**, *80*, 214427.
(6) Józsa, C.; Maassen, T.; Popinciuc, M.; Zomer, P. J.; Veligura, A.; Jonkman, H. T.; van Wees, B. J. *Phys. Rev. B* **2009**, *80*, 241403.
(7) Maassen, T.; Dejene, F. K.; Guimarães, M. H. D.; Józsa, C.; van Wees, B. J. *Phys. Rev. B* **2011**, *83*, 115410.
(8) Han, W.; Pi, K.; Bao, W.; McCreary, K. M.; Li, Y.; Wang, W. H.; Lau, C. N.; Kawakami, R. K. *Appl. Phys. Lett.* **2009**, *94*, 222109.
(9) Han, W.; Pi, K.; McCreary, K. M.; Li, Y.; Wong, J. J. I.; Swartz, A. G.; Kawakami, R. K. *Phys. Rev. Lett.* **2010**, *105*, 167202.
(10) Han, W.; Kawakami, R. K. *Phys. Rev. Lett.* **2011**, *107*, 047207.
(11) Maassen, T.; van den Berg, J. J.; IJbema, N.; Fromm, F.; Seyller, T.; Yakimova, R.; van Wees, B. J. *Nano Lett.* **2012**, *12*, 1498–1502.
(12) Wojtaszek, M.; Vera-Marun, I. J.; Maassen, T.; van Wees, B. J. *Phys. Rev. B* **2013**, *87*, 081402.
(13) Volmer, F.; Drögeler, M.; Maynicke, E.; von den Driesch, N.; Boschen, M. L.; Güntherodt, G.; Stampfer, C.; Beschoten, B. *Phys. Rev. B* **2014**, *90*, 165403.
(14) Guimarães, M. H. D.; Veligura, A.; Zomer, P. J.; Maassen, T.; Vera-Marun, I. J.; Tombros, N.; van Wees, B. J. *Nano Lett.* **2012**, *12*, 3512–3517.
(15) Zomer, P. J.; Guimarães, M. H. D.; Tombros, N.; van Wees, B. J. *Phys. Rev. B* **2012**, *86*, 161416.
(16) Dlubak, B.; Martin, M.-B.; Deranlot, C.; Servet, B.; Xavier, S.; Mattana, R.; Sprinkle, M.; Berger, C.; De Heer, W. A.; Petroff, F.; Anane, A.; Seneor, P.; Fert, A. *Nat. Phys.* **2012**, *8*, 557–561.
(17) Wang, W. H.; Han, W.; Pi, K.; McCreary, K. M.; Miao, F.; Bao, W.; Lau, C. N.; Kawakami, R. K. *Appl. Phys. Lett.* **2008**, *93*, 183107.
(18) Wang, L.; Meric, I.; Huang, P. Y.; Gao, Q.; Gao, Y.; Tran, H.; Taniguchi, T.; Watanabe, K.; Campos, L. M.; Muller, D. A.; Guo, J.;

Kim, P.; Hone, J.; Shepard, K. L.; Dean, C. R. *Science* **2013**, *342*, 614−617.
(19) Lee, J. E.; Ahn, G.; Shim, J.; Lee, Y. S.; Ryu, S. *Nat. Commun.* **2012**, *3*, 1024.
(20) Stampfer, C.; Molitor, F.; Graf, D.; Ensslin, K.; Jungen, A.; Hierold, C.; Wirtz, L. *Appl. Phys. Lett.* **2007**, *91*, 241907.
(21) Peres, N. M. R. *Rev. Mod. Phys.* **2010**, *82*, 2673−2700.
(22) Das Sarma, S.; Adam, S.; Hwang, E. H.; Rossi, E. *Rev. Mod. Phys.* **2011**, *83*, 407−470.
(23) Huertas-Hernando, D.; Guinea, F.; Brataas, A. *Phys. Rev. Lett.* **2009**, *103*, 146801.
(24) Gorbachev, R. V.; Riaz, I.; Nair, R. R.; Jalil, R.; Britnell, L.; Belle, B. D.; Hill, E. W.; Novoselov, K. S.; Watanabe, K.; Taniguchi, T.; Geim, A. K.; Blake, P. *Small* **2011**, *7*, 465−468.
(25) Details on the measurement technique can be found in ref 4.
(26) In contrast to graphene that was directly deposited onto Si/SiO_2, we have to consider an additional dielectric (air) between the graphene and the surface of the substrate as well as the partial shielding of the electric field by the nearby electrodes. We therefore simulate the capacitive coupling of our devices using Comsol for both suspended and nonsuspended regions with different electrode spacings that gives an estimate for α.
(27) Jedema, F. J.; Heersche, H. B.; Filip, A. T.; Baselmans, J. J. A.; van Wees, B. J. *Nature* **2002**, *416*, 713−716.
(28) Lou, X.; Adelmann, C.; Crooker, S. A.; Garlid, E. S.; Zhang, J.; Reddy, K. S. M.; Flexner, S. D.; Palmstrom, C. J.; Crowell, P. A. *Nat. Phys.* **2007**, *3*, 197−202.
(29) Torrey, H. C. *Phys. Rev.* **1956**, *104*, 563−565.
(30) Johnson, M.; Silsbee, R. H. *Phys. Rev. B* **1988**, *37*, 5312−5325.
(31) Fabian, J.; Matos-Abiague, A.; Ertler, C.; Stano, P.; Žutić, I. *Acta Phys. Slovaca* **2007**, *57*, 565−907.
(32) Han, W.; Chen, J.-R.; Wang, D.; McCreary, K. M.; Wen, H.; Swartz, A. G.; Shi, J.; Kawakami, R. K. *Nano Lett.* **2012**, *12*, 3443−3447.
(33) Zhang, P.; Wu, M. W. *Phys. Rev. B* **2011**, *84*, 045304.
(34) Zhang, P.; Wu, M. W. *New J. Phys.* **2012**, *14*, 033015.
(35) Diez, M.; Burkard, G. *Phys. Rev. B* **2012**, *85*, 195412.
(36) Childres, I.; Jauregui, L. A.; Foxe, M.; Tian, J.; Jalilian, R.; Jovanovic, I.; Chen, Y. P. *Appl. Phys. Lett.* **2010**, *97*, 173109.
(37) Yuasa, S.; Fukushima, A.; Kubota, H.; Suzuki, Y.; Ando, K. *Appl. Phys. Lett.* **2006**, *89*, 042505.
(38) Varykhalov, A.; Marchenko, D.; Sánchez-Barriga, J.; Scholz, M. R.; Verberck, B.; Trauzettel, B.; Wehling, T. O.; Carbone, C.; Rader, O. *Phys. Rev. X* **2012**, *2*, 041017.
(39) Guimarães, M. H. D.; Zomer, P. J.; Ingla-Aynés, J.; Brant, J. C.; Tombros, N.; van Wees, B. J. *Phys. Rev. Lett.* **2014**, *113*, 086602.